

1 **ASSIMILATING REMOTELY SENSED CLOUD OPTICAL THICKNESS INTO A**  
2 **MESOSCALE MODEL**

3  
4  
5  
6  
7 Lauwaet D.\*<sup>1,2</sup>, De Ridder K.<sup>2</sup>, Pandey P.,<sup>1,2</sup>  
8  
9

10  
11  
12  
13 <sup>1</sup>Physical and Regional Geography Research Group  
14 Department of Earth and Environmental Sciences  
15 K.U.Leuven  
16 Celestijnenlaan 200 E  
17 3001 Heverlee  
18 Belgium  
19

20  
21  
22  
23  
24 <sup>2</sup>Vlaamse Instelling voor Technologisch Onderzoek (VITO)  
25 Boeretang 200  
26 2400 Mol  
27 Belgium  
28

29  
30  
31  
32  
33  
34 Research article  
35  
36  
37  
38  
39  
40  
41  
42  
43  
44  
45  
46  
47  
48  
49  
50

51 \*Corresponding author: tel: +32 16 32 64 26  
52 fax: +32 16 32 29 80  
53 e-mail: [dirk.lauwaet@ees.kuleuven.be](mailto:dirk.lauwaet@ees.kuleuven.be)  
54

1 **ABSTRACT:**

2

3 The Advanced Regional Prediction System, a mesoscale atmospheric model, is applied to  
4 simulate the month of June 2006 with a focus on the near surface air temperatures around  
5 Paris. To improve the simulated temperatures which show errors up to 10 K during a day on  
6 which a cold front passed Paris, a data assimilation procedure to calculate 3D analysis fields  
7 of specific cloud liquid and ice water content is presented. The method is based on the  
8 assimilation of observed cloud optical thickness fields into the Advanced Regional Prediction  
9 System model and operates on 1D vertical columns, assuming that the horizontal background  
10 error covariance is infinite, i.e. an independent pixel approximation. The rationale behind it is  
11 to find vertical profiles of cloud liquid and ice water content that yield the observed cloud  
12 optical thickness values and are consistent with the simulated profile. Afterwards, a latent heat  
13 adjustment is applied to the temperature in the vertical column. Data from several  
14 meteorological stations in the study area are used to verify the model simulations. The results  
15 show that the presented assimilation procedure is able to improve the simulated 2 m air  
16 temperatures and incoming shortwave radiation significantly during cloudy days. The scheme  
17 is able to alter the position of the cloud fields significantly and brings the simulated cloud  
18 pattern closer to the observations. As the scheme is rather simple and computationally  
19 inexpensive, it is a promising new technique to improve the surface fields of retrospective  
20 model simulations for variables that are affected by the position of the clouds.

21

22 **KEYWORDS:** ARPS, cloud optical thickness, data assimilation, optimal interpolation.

23

## 1 **1. Introduction**

2

3 Mesoscale atmospheric models are used extensively to reconstruct high-resolution regional  
4 atmospheric conditions as an input for e.g. hydrological, land surface or air pollution models.

5 Although sophisticated techniques are used to parameterize clouds and precipitation, a large  
6 source of uncertainty in the model results remains in predicting the location of cloud systems

7 at high spatial resolutions. As clouds have a strong impact on the surface energy budget and  
8 hence the local temperatures, an inaccurate simulation of the overlying cloud cover is

9 problematic for certain applications that need correct surface input data. The assimilation of  
10 satellite data into the atmospheric model can play an important role in providing improved

11 model results on a local scale.

12

13 Cloud assimilation studies have focused mainly on cloud retrievals from radar data, either  
14 with one-dimensional variational schemes (1DVAR) (Benedetti et al., 2003) or with more

15 complex models in 3DVAR (Hu et al., 2006a,b) and 4DVAR (Sun and Crook, 1998;  
16 Vukićević et al., 2004). Recently, Benedetti and Janisková (2008) used a 4DVAR system to

17 assimilate Moderate Resolution Imaging Spectroradiometer (MODIS) cloud optical depth  
18 observations into the European Centre for Medium range Weather Forecast (ECMWF) model.

19 Their results show a positive impact on certain variables like the distribution of cloud ice  
20 water content but the assimilation did not always improve the analysis fit to the observations.

21 However, the large computational infrastructure needed to run and maintain these systems are  
22 limiting their use for smaller research centres and universities.

23

24 Other simpler and faster methods exist that attempt to retrieve model cloud microphysics from  
25 satellite observations or other sources. Soutu et al. (2003) constructed cloud fields for their

1 forecasts over the Galician Region in Spain based on relative humidity values from the NCEP  
2 Aviation Model. Their procedure followed the Local Analysis and Prediction System (LAPS,  
3 Albers et al., 1996) and clearly improved the model's skill to predict precipitation amounts.  
4 Another method is used by Yucel et al. (2003), who applied a nudging assimilation technique  
5 to ingest remotely sensed cloud cover and cloud top height data into their mesoscale  
6 atmospheric model. The cloud ingestion was found to improve the ability of the model to  
7 capture the variation in surface fields associated with cloud cover. However, they suggested  
8 that it would be necessary to modify the model dynamics and thermodynamics to be  
9 consistent with the ingested cloud fields.

10

11 In this context, the goal of the research reported here is to present a rather simple and  
12 computational fast cloud assimilation scheme. The scheme applies optimal interpolation with  
13 latent heat adjustment for the assimilation of cloud optical thickness (COT) observations into  
14 a mesoscale atmospheric model to study the effect on the simulated surface fields associated  
15 with cloud cover. The model used for this study is the Advanced Regional Prediction System  
16 (ARPS), a non-hydrostatic mesoscale atmospheric model developed at the University of  
17 Oklahoma (Xue et al., 2000; Xue et al., 2001). Although the ARPS model has its own cloud  
18 analysis package (ADAS, Brewster, 1996), it is not used in our study. ADAS needs  
19 information on the vertical extent of the clouds to estimate cloud types and related in-cloud  
20 vertical velocities which can not be derived from our two-dimensional cloud optical thickness  
21 data.

22

23 The remainder of the paper is organized as follows. A description of the atmospheric model  
24 and a set-up for the model simulations are given in section 2. In section 3, the details of the

1 cloud assimilation scheme are presented. The results are evaluated and discussed in section 4  
2 while conclusion are given in section 5.

3

## 4 **2. Numerical model and data description**

5

6 The Advanced Regional Prediction System (ARPS) includes conservation equations for  
7 momentum, heat, mass, water (vapour, liquid and ice), sub-grid scale turbulent kinetic energy  
8 and the state-equation of moist air. The finite-difference equations of the model are  
9 discretized on an Arakawa C-grid, employing a terrain following coordinate in the vertical  
10 direction. Advection is solved with a fourth-order central differencing scheme and leapfrog  
11 time stepping. Turbulence is represented by the 1.5-order turbulent kinetic energy (TKE)  
12 model, and the Sun and Chang (1986) parameterization for the convective boundary layer.  
13 The 6-category water/ice scheme of Lin et al. (1983) accounts for the model microphysics  
14 while the Kain-Fritsch cumulus parameterization scheme solves the cumulus convection  
15 (Kain and Fritsch, 1990). In order to suppress numerical noise, a fourth-order monotonic  
16 computational mixing was applied, following Xue (2000).

17

18 Land surface processes are parameterized by the Soil-Vegetation-Atmosphere Transfer model  
19 of De Ridder and Schayes (1997). The two primary parameters of the land surface model are  
20 the type of vegetation, which is derived from the Coordination Information Environment  
21 (CORINE) land cover data and the soil texture, which is assumed to be that of a loamy soil,  
22 homogeneous across the domain. Among the secondary parameters, vegetation fraction is  
23 based on the normalized difference vegetation index (NDVI) from the SPOT-VEGETATION  
24 satellite imagery.

25

1 Data with a  $0.25^\circ$  horizontal resolution from the global operational analysis by the ECMWF  
2 are used as initial conditions and as 6-hourly lateral boundary conditions for the model runs.  
3 The ARPS model domain has a grid spacing of 16 km and a domain size of 1600 km  $\times$  1600  
4 km, centred over Paris (Figure 1). In all simulations, 35 vertical levels are employed with a  
5 grid spacing of 25 m near the surface increasing to 1 km near the upper model boundary,  
6 located at 20 km altitude. The simulations are initialized on 1 June 2006 at 0000 LT and run  
7 until 30 June 2006 at 2400 LT. This month is chosen to test our assimilation scheme as during  
8 some periods of this month, the model has problems in simulating the right amount and  
9 position of clouds, which leads to large errors in some surface variables as will be shown in  
10 section 4.

11  
12 The cloud optical thickness images for June 2006 are retrieved from visible and shortwave  
13 infrared imagery from the Spinning Enhanced Visible and InfraRed Imager (SEVIRI) onboard  
14 the Meteosat Second Generation satellite with a semi-analytical cloud retrieval algorithm  
15 (Pandey et al., 2011). This algorithm is based on the retrieval algorithm of Kokhanovsky et al.  
16 (2003) for the estimation of cloud optical thickness. The details of the scheme can be found in  
17 Pandey et al. (2011). As Meteosat is a geostationary satellite, the algorithm provides COT  
18 images every quarter of an hour during daytime (0600-2000 LT). These images are  
19 assimilated every 15 minutes into the ARPS model following the procedure that is explained  
20 in section 3.

21  
22 To test the effect of our cloud assimilation procedure, 2 m air temperature and specific  
23 humidity data for 2 observational stations close to Paris (Melun and Trappes) and a station in  
24 Bordeaux are gathered from the National Climatic Data Center (NCDC) dataset (Figure 1).  
25 Furthermore, 2 m air temperature, specific humidity and incoming shortwave radiation data

1 for 3 more stations (Fontainbleau, Grignon and Oensingen, Figure 1) are taken from the  
2 CarboEurope Integrated Project.

3

### 4 **3. Cloud optical thickness assimilation procedure**

5

6 The data assimilation procedure applied in this study calculates 3D analysis fields of specific  
7 cloud liquid and ice water content ( $q_c$  and  $q_i$ ) and operates on 1D vertical columns. The  
8 rationale behind the method is to find vertical profiles of  $q_c$  and  $q_i$  that yield the observed  
9 cloud optical thickness fields  $\tau_\theta$ , and that are consistent with the background (simulated)  
10 profile, in the sense that clouds are put in layers with a large humidity. This a priori  
11 assumption is required as  $\tau_\theta$  does not contain height information.

12

#### 13 *3.1 Background COT*

14

15 Consider a vertical model column containing n grid cells irregularly spaced at positions  $z_i$   
16 ( $i=1,\dots,n$ ), starting from the surface. Each layer (thickness  $\Delta z_i$ ) is characterized by a simulated  
17 specific cloud water content  $q_{cbi}$ , which can be either liquid or solid (ice) water. Noting that  
18 the quantity  $\rho_i q_{cbi} \Delta z_i$  is the incremental liquid/ice water path (in  $\text{kg m}^{-2}$ ) of layer  $i$  ( $\rho_i$  being the  
19 air density of layer  $i$ ), the incremental optical depth contributed by layer  $i$  is given by  
20 (Kokhanovsky, 2006):

21

$$\Delta\tau_{bi} = \frac{3}{2\rho_w} \frac{\rho_i q_{cbi}}{r_{ei}} \Delta z_i$$

22

23 with  $\rho_w = 1000 \text{ kg m}^{-3}$  the density of liquid water, and  $r_{ei}$  the effective radius of cloud droplets  
24 in layer  $i$ , which is parameterized in ARPS as a function of temperature, to account for the

1 different values of this quantity for liquid versus solid water. The subscript b denotes the  
 2 background fields. A list of all the symbols is provided in Appendix A.

3

4 The full model-based columnar optical depth is then given by:

$$\begin{aligned}
 \tau_b &= \sum_{i=1}^n \Delta \tau_{bi} \\
 &= \frac{3}{2\rho_w} \sum_{i=1}^n \frac{\rho_i q_{cbi}}{r_{ei}} \Delta z_i \\
 &= \frac{3}{2\rho_w} \left( \frac{\rho_1 \Delta z_1}{r_{e1}} \dots \frac{\rho_n \Delta z_n}{r_{en}} \right) \begin{pmatrix} q_{cb1} \\ \vdots \\ q_{cbn} \end{pmatrix} \\
 &\equiv \mathbf{H} \mathbf{q}_{cb}
 \end{aligned}$$

5

6  $\mathbf{H}$  is a so-called observation operator, which linearly maps  $\mathbf{q}_{cb}$  onto a background (i.e.,  
 7 simulated) optical thickness ( $\tau_b = \mathbf{H} \mathbf{q}_{cb}$ ).

8

### 9 *3.2 Optimal interpolation*

10

11 Given observations of cloud optical thickness for a given position on the globe, the best linear  
 12 unbiased estimate of cloud water content is given by (Kalnay, 2003):

13

$$q_{ca} = q_{cb} + \mathbf{K}(\tau_0 - \mathbf{H}q_{cb})$$

14

1 with  $\mathbf{q}_{ca}$  the vector containing the analyzed cloud water content values at level  $i$ , and  $\mathbf{q}_{cb}$   
 2 likewise containing the values generated by the model ('background' or first guess value).  
 3 The gain matrix is given by

$$K = \mathbf{B}\mathbf{H}^T(\mathbf{H}\mathbf{B}\mathbf{H}^T + \mathbf{R})^{-1}$$

4  
 5  
 6 with  $\mathbf{B}$  the background error covariance matrix and  $\mathbf{R} (\equiv \sigma_\tau^2)$  the observation error covariance,  
 7 which in this case is a scalar since  $\tau_o$  itself is a scalar quantity.

8  
 9 We will assume that  $\mathbf{B}$  is a diagonal matrix. This is not entirely realistic, since errors of cloud  
 10 water content at different vertical layers may be correlated, especially if these layers are close  
 11 to each other in comparison to the typical thickness of a cloud layer. Nevertheless, it is  
 12 difficult to estimate these inter-layer correlations and, moreover, the thicknesses of the layers  
 13 that are prone to cloud development (sufficiently far away from the surface) are rather thick,  
 14 thus making this diagonality assumption less of a problem. A diagonal background error  
 15 covariance matrix has the advantage of leading to a fairly simple final expression for the  
 16 analyzed specific cloud water content, as shown below. In Appendix B, the results of a test  
 17 with a non-diagonal  $\mathbf{B}$  matrix are presented in order to have an estimate of the impact of this  
 18 assumption.

19  
 20 Thus, in case  $\mathbf{B}$  is a diagonal matrix with elements  $\sigma_{ci}^2 \delta_{ij}$  (with  $\delta_{ij}$  the Kronecker delta), one  
 21 has:

$$\mathbf{H}\mathbf{B}\mathbf{H}^T + \mathbf{R} = \sum_{i=1}^n \sigma_{ci}^2 h_i^2 + \sigma_\tau^2$$

$$\mathbf{BH}^T = (\sigma_{c1}^2 h_1 \dots \sigma_{cn}^2 h_n)^T$$

1

2 with  $h_i$  the operation operator for layer  $i$ . This leads, finally, to:

3

$$q_{cai} = q_{cbi} + \frac{\sigma_{ci}^2 h_i}{\sum_{i=1}^n \sigma_{ci}^2 h_i^2 + \sigma_{\tau}^2} \left( \tau_0 - \sum_{i=1}^n h_i q_{cbi} \right)$$

4

5 The main challenge is to specify the  $\sigma_{ci}$  in a suitable manner, in particular in such a way that  
6 model layers with a high simulated humidity are more affected than the drier layers.

7

### 8 *3.3 Cloud water background error variance*

9

10 The specification of the cloud water background error variance  $\sigma_{ci}$  of each model layer is not  
11 straightforward, in particular when a layer contains no simulated liquid or ice water ( $q_{cbi} = 0$ ).

12 One might be tempted to set  $\sigma_{ci} = 0$  in such a situation, but from the analysis equation above it  
13 is clear that  $q_{cai}$  will also be zero then, even if a cloud is observed ( $\tau_o > 0$ ). Clearly, a non-zero  
14 cloud water background error variance must be assigned, even for non-saturated layers.

15 Simply taking  $\sigma_{ci}$  as a fraction of  $q_{cbi}$  will not work for the reasons just explained. The  
16 background error variance matrix will therefore be established starting from a probability  
17 density function for total specific water content  $q_t$ , which is defined as the sum of vapour and  
18 cloud (liquid/ice) contributions, i.e.,  $q_t = q_v + q_c$ . It should be noted that by assigning a cloud  
19 variance to a non-cloudy background layer, the analysis implicitly allows to adjust the water  
20 vapour profile in absence of background clouds. The goal is now to find the cloud water  
21 content error, given the error on total water content. The error on the latter needs to be

1 specified a priori, in our case this will be done as a fixed fraction of total water content (see  
 2 Section 3.4).

3

4 We employ a normal distribution, given by:

5

$$f(q_t) = \frac{1}{\sqrt{2\pi}\sigma_t} e^{-\frac{(q_t - q_{tb})^2}{2\sigma_t^2}}$$

6

7 with  $q_{tb}$  the background (simulated) value of  $q_t$ , and  $\sigma_t$  the standard deviation of the  
 8 distribution, which is a measure for the error on simulated total water  $q_t$ . Figure 2 presents the  
 9 concept of the normal distribution of  $q_t$ .

10

11 Cloud water is that portion of  $q_t$  which is in excess of the saturated value, denoted  $q_s$   
 12 ( $\equiv q_{sat}(T)$ ), with  $T$  the temperature of the considered layer, so that  $q_c = (q_t - q_s)H(q_t - q_s)$ , with  $H(\cdot)$   
 13 the Heaviside step function, which is unity for a positive argument and zero otherwise. Using  
 14 this, taking the simulated cloud water content  $q_{cb}$  as expected value for this quantity, and  
 15 omitting the layer index  $i$  for the moment, the error variance of simulated cloud water can be  
 16 calculated as follows:

17

$$\begin{aligned} \sigma_c^2 &= \int_{-\infty}^{+\infty} (q_c - q_{cb})^2 f(q_t) dq_t \\ &= \int_{q_s}^{+\infty} [(q_c + q_s) - (q_{cb} + q_s)]^2 f(q_t) dq_t \\ &= \int_{q_s}^{+\infty} (q_t - q_{tb})^2 f(q_t) dq_t \end{aligned}$$

1 such that:

2

$$\begin{aligned}\sigma_c^2 &= \frac{1}{\sqrt{2\pi}\sigma_t} \int_{q_s}^{+\infty} (q_t - q_{tb})^2 e^{-\frac{(q_t - q_{tb})^2}{2\sigma_t^2}} dq_t \\ &= \frac{2\sigma_t^2}{\sqrt{\pi}} \int_{x_s}^{+\infty} x^2 e^{-x^2} dx \\ &= \sigma_t^2 \left[ \frac{1}{2} \operatorname{erfc}(x_s) + \frac{x_s}{\sqrt{\pi}} e^{-x_s^2} \right]\end{aligned}$$

3

4 with  $x_s = \frac{(q_s - q_{tb})}{\sqrt{2}\sigma_t}$  and  $\operatorname{erfc}(\cdot)$  the complementary error function. It should be noted that in  
5 these formulas the error on the background saturated specific humidity, hence the background  
6 temperature field, is ignored to simplify the assimilation scheme. In Appendix C, the effect of  
7 this approximation is assessed and it is shown that it does not have a significant effect on the  
8 outcome of the assimilation procedure.

9

### 10 *3.4 Implementation in the ARPS model*

11

12 In the above, the standard deviation on the simulated total water content and the observed  
13 cloud optical thickness are still unknown. These standard deviations are expressed as a  
14 fraction of  $q_t$  and  $\tau_0$ , respectively, i.e.  $\sigma_t = a q_t$  and  $\sigma_\tau = b \tau_0$ . In our study, a value of 0.3 is  
15 adopted for coefficient  $a$  (i.e.,  $\pm 30\%$  error of  $q_t$ ). This value is obtained from a comparison  
16 between modelled and observed specific humidity profiles at Trappes, as more than 80 % of  
17 the observed data points are within this error margin of the simulated profiles. For coefficient  
18  $b$ , a rather conservative value of 0.25 is adopted (i.e.  $\pm 25\%$  error of  $\tau_0$ ), with a lower limit of  
19 5 for  $\sigma_\tau$ , based on a validation study of our cloud optical thickness product with Cloudsat

1 COT data (Pandey et al., 2011). To test the sensitivity of the assimilation procedure to these  
2 two coefficients, a sensitivity study is performed by varying the values between 0.1 and 0.5.  
3 The results are presented at the end of section 4.2.

4  
5 The resulting  $q_{ca}$  from the assimilation procedure is defined as cloud liquid water when the  
6 temperature is warmer than  $-10^{\circ}\text{C}$ , and as cloud ice when the temperature is colder than -  
7  $30^{\circ}\text{C}$ . A linear ramp is applied for the temperature in between. Whenever a non-saturated (and  
8 cloudless) layer becomes cloudy after the analysis, the specific humidity is set to its saturated  
9 value. Last, a latent heat adjustment to temperature based on the added or subtracted amounts  
10 of  $q_c$  and  $q_i$  is applied, according to the formula:

$$\Delta T_{qc} = \Delta q_c \frac{L_v}{C_p}$$
$$\Delta T_{qi} = \Delta q_i \frac{L_v + L_f}{C_p}$$

12  
13 where  $L_v$  and  $L_f$  are the latent heat of vaporization and fusion at  $0^{\circ}\text{C}$  respectively, and  $C_p$  is the  
14 specific heat of dry air at constant pressure.

#### 15 16 **4. Results of the assimilation procedure**

17  
18 This section describes the results for a COT assimilation experiment (EXP) for the month of  
19 June 2006, compared to a reference simulation (REF) with a setup identical to the cloud  
20 assimilation experiment to provide a benchmark for the effect of the introduction of cloud  
21 optical thickness data.

22

#### 1 *4.1 Comparison to observations*

2

3 Figure 3 shows the impact of the COT assimilation on 2 m air temperatures, measured at  
4 Melun and Oensingen (locations in Figure 1). It is apparent that the reference simulation does  
5 not correctly capture a sharp temperature decrease halfway through the month (Julian day 166  
6 in Melun and 168 in Oensingen) and keeps on overestimating the temperatures around noon  
7 by a few degrees during the rest of the month. This is substantially improved by the COT  
8 assimilation which picks up these temperature decreases on the respective days and the  
9 following period. The problems for the reference simulation are caused by a wrong location of  
10 a cold front and associated overlying cloud cover during these days, as will be shown later on.  
11 The assimilation procedure is thus capable of improving the cloud fields and yielding more  
12 accurate temperature values. Note that sometimes also the temperature during night time  
13 improves in the EXP simulation (e.g. on Julian day 177 in Melun) although the assimilation  
14 scheme is only active during day time (as satellite data from a visible channel are needed to  
15 derive COT). This is due to the transportation of the assimilated moisture throughout the  
16 model domain.

17

18 These findings are further demonstrated in Table 1, which shows the results for 4 of the  
19 observation stations throughout the model domain. The COT assimilation reduces the root-  
20 mean-square error (RMSE) between modelled and observed values for all stations. Also the  
21 correlation coefficients between the modelled and observed time series are higher for the  
22 assimilation experiment. The positive bias for the stations around Paris that is present in the  
23 reference simulation is decreased. However, there is a slight negative effect of the  
24 assimilation on the biases in Oensingen en Bordeaux. Overall, the statistics of these time  
25 series are clearly improved by the assimilation.

1

2 Another variable that is closely linked to the cloud fields, is the surface shortwave radiation.

3 The results for the observation stations of Grignon, Fontainbleau and Oensingen are presented

4 in Figure 4 and Table 2. As for the temperature, the COT assimilation experiment clearly

5 improves the time series, especially on the problematic Julian days 166 (Grignon) and 173

6 (Grignon and Oensingen). The statistics show a substantial reduction of the bias and RMSE

7 and higher correlation coefficients. These numbers confirm that the improvement in the

8 assimilation experiment is linked to a better position of the cloud cover in the model.

9

10 However, the impact of the COT assimilation is not positive for all variables, as shown in

11 Table 3. The specific humidity at the surface is in good agreement with the observations for

12 the reference simulation, whereas it is overestimated by about  $1 \text{ g kg}^{-1}$  for most observation

13 stations when the assimilation scheme is applied. Only in Oensingen, the assimilation

14 improves the underestimated humidity in the reference simulation. The extra moisture is

15 caused by the fact that the assimilation scheme sets the humidity of a layer to its saturated

16 value whenever a non-saturated layer becomes cloudy. As the reference simulation

17 underestimates the amount of clouds compared to the observations, an increase of the

18 humidity is the logical consequence in this case. This can not be avoided if we want to retain

19 the assimilated clouds, otherwise they would evaporate instantly. In their cloud assimilation

20 experiments, Benedetti and Janiskova (2008) also noticed that the humidity was affected in a

21 slightly negative way by the assimilation.

22

23 In order to evaluate the effect of the assimilation on the vertical distributed moisture, the total

24 water columns from radio-soundings launched at Trappes are compared to the reference and

25 assimilation experiments (Figure 5). Overall, there is a good agreement between model results

1 and observations, as the mean RMSEs of both the REF and EXP simulations are only 4 mm.  
2 The assimilation scheme has only a small impact on the total water column and slightly  
3 improves the small negative model bias. So the problems with the humidity that are  
4 mentioned before are limited and do not translate in drastic changes in the total vertical  
5 moisture amounts.

6

#### 7 *4.2 Impact on temperature, humidity and cloud parameters*

8

9 To assess the impact of the assimilation procedure on the model variables in the entire model  
10 domain, mean zonal differences between the experiment and the reference for temperature,  
11 specific humidity and vertical wind speed are shown in Figure 6. The assimilation clearly has  
12 the largest effect in the lowest 2000 m of the model domain for both the temperature and  
13 specific humidity. Here, the temperature values of the experiment have a tendency to be lower  
14 (up to 0.5 K) while the specific humidity is augmented (up to 0.5 g kg<sup>-1</sup>). Both temperature  
15 and moisture changes are in phase to enhance cloud formation. In the upper levels, a slight  
16 temperature increase is visible for the assimilation experiment, which is caused by latent heat  
17 release during the formation of additional clouds. As shown in the previous section, the  
18 temperature decrease near the surface improves the positive bias in the reference simulation,  
19 while the moisture increase has a negative effect when compared to the observations.

20

21 Regarding the vertical wind speed, the largest changes clearly occur in the southern part of the  
22 model domain where most extra water is added to the model (see Figure 7). The enhanced  
23 convection and latent heat release causes more updrafts in the higher model layers and  
24 downdrafts close to the surface. It should be noted that these changes are rather small (less  
25 than 10 %) in comparison to the mean vertical wind speeds. As a response to the changes

1 induced by the assimilation scheme, there is a noticeable redistribution in liquid water path  
2 and ice water path in the model domain (Figure 7). The changes appear to have a rather varied  
3 structure over the largest part of the model domain. Most increases occur along the southern  
4 boundary of the domain and over the alpine region. Overall, there is a clear tendency of  
5 increased cloud amounts in the assimilation experiment. The monthly mean values of the  
6 liquid and ice water paths are raised by 25 and 8 % respectively. Regarding the  
7 overestimation of incoming shortwave radiation by the reference simulation (Table 2), these  
8 changes appear to have a positive impact on the model results. The assimilation also has an  
9 impact on the modelled rainfall amounts with a logical positive trend in the regions where  
10 more cloud ice is produced (last panel of Figure 7). The overall effect is relatively large as the  
11 monthly mean rainfall is increased by 26 %, although it should be noted that this is a dry  
12 month where eventual changes have a strong effect on the overall statistics.

13  
14 The direct impact of the COT assimilation on the modelled cloud fields is presented in Figure  
15 8. In this figure the position of the clouds is shown on 15 July at noon, when a cold front  
16 passes Paris which is not picked up in the reference simulation (Figure 3). The top two panels  
17 of the figure show a comparison between the cloud optical thickness product of the Moderate  
18 Resolution Imaging Spectroradiometer (MODIS) and our product from MSG Seviri. The  
19 positions of the clouds in both images are clearly very similar, although the mean COT value  
20 of MODIS is 18 % higher than the MSG Seviri value. For the reference simulation, the clouds  
21 are positioned too far to the east and there is no strong front structure visible. The COT  
22 assimilation scheme is able to alter the cloud structure significantly and brings it much closer  
23 to the observations over the central region of the model domain. Although the scheme is not  
24 able to get rid entirely of the overestimation of clouds in the west side of the model domain, it  
25 is clearly able to improve the model simulation.

1  
2  
3  
4  
5  
6  
7  
8  
9  
10  
11  
12  
13  
14  
15  
16  
17  
18  
19  
20  
21  
22  
23  
24  
25

Finally, the sensitivity of the assimilation scheme to the coefficients  $a$  and  $b$ , related to the standard deviation of the simulated total water content and the observed cloud optical thickness, respectively, is tested. The results of this sensitivity experiment on the statistics for Melun are presented in Table 4. The values of these parameters have an effect on the model results and the scheme seems a little more sensitive to  $\sigma_t$ . Considering the results of both the temperature and humidity at the surface for this station, the initial choice of the values for  $a$  and  $b$  seems accurate as none of the sensitivity experiments can improve on these results.

**5. Discussion and conclusions**

In this paper, a technique has been presented to assimilate cloud optical thickness information into a mesoscale atmospheric model to yield improved diagnoses of surface solar radiation and temperature. The technique comprises an optimal interpolation of cloud liquid and ice water in 1D vertical columns together with a latent heat adjustment. The scheme requires some assumptions including an independent pixel approximation, but it is rather simple and computationally inexpensive, especially when compared to the 4DVAR systems that are currently developed (e.g. Benedetti and Janisková, 2008). The goal of the assimilation scheme is to improve retrospective model simulations by feeding the model with observed cloud optical thickness images every 15 minutes.

Results for the month of June 2006 show a positive impact of the assimilation on near-surface temperatures and incoming shortwave radiation, two variables that are closely linked to the overlying cloud cover and are crucial as input in, for instance, air pollution models. However, comparison to specific humidity observations show that the changes induced by the

1 assimilation do not always improve the model fit to the observations. The assimilation scheme  
2 tends to induce overestimations of humidity close to the surface due to the fact that a layer is  
3 set to saturation when it becomes cloudy. This is necessary to retain the new clouds in the  
4 model and the same technique is used in the cloud analysis scheme of Soutu et al. (2003).  
5 Although the moisture field in the lowest 2000 m of the model domain is affected in a slightly  
6 negative way, the results show that the position of the cloud fields are more accurately  
7 simulated when the cloud observations are assimilated.

8

9 We can thus conclude that it is feasible to introduce the presented COT assimilation  
10 procedure in a mesoscale atmospheric model. The results show that the benefits of the  
11 assimilation to the surface temperature and radiation fields outweigh eventual inconsistencies  
12 that are caused by only adjusting the moisture and temperature fields of the model. As the  
13 procedure is simple and fast, it is a promising new technique to improve the quality of surface  
14 level model output of retrospective simulations.

15

16

1 **Acknowledgements**

2 This research has been performed in the framework of the Climate and Air Quality Modelling  
3 for Policy Support (Climaqs) project, sponsored by the Flemish agency for Innovation by  
4 Science and Technology, and the FP-7 Myair PASODOBLE project, sponsored by the  
5 European Commission's Seventh Framework Programme. We would like to thank the  
6 following CARBOEUROPE PIs for providing access to their data: Jean-Yves Pontailier (FR-  
7 FON), Nicolas Mascher (FR-GRI) and Cristof Ammann et al. (SWI-OEN). We also  
8 acknowledge the National Climatic Data Center (NCDC) for providing valuable validation  
9 data. The ARPS meteorological model was made available by the Center for Analysis and  
10 Prediction of Storms at the University of Oklahoma. We would also like to acknowledge the  
11 European Environment Agency for making available the CORINE land-cover data, the U.S.  
12 Geological Survey for the GTOPO30 dataset, the Jet Propulsion Laboratory for the SST  
13 imagery, NASA's Earth Science Division for the GLDAS data, and our VITO colleagues at  
14 TAP for the SPOT-VEGETATION NDVI imagery. Meteorological forcing data were  
15 obtained from the European Centre for Medium-Range Weather Forecasting (ECMWF).

16

## 1 Appendix A: List of Symbols

a	coefficient in relation to $\sigma_t$ (-)
b	coefficient in relation to $\sigma_\tau$ (-)
<b>B</b>	background error covariance matrix
$C_p$	specific heat of air at constant pressure ( $J\ kg^{-1}\ K^{-1}$ )
erfc	complementary error function
<b>H</b>	observation operator matrix
H	heaviside step function
<b>H<sup>T</sup></b>	transposed observation operator matrix
<b>K</b>	gain matrix
$L_f$	latent heat of fusion ( $J\ kg^{-1}$ )
$L_v$	latent heat of vaporization ( $J\ kg^{-1}$ )
q	specific humidity ( $kg\ kg^{-1}$ )
$q_c$	specific cloud liquid water content ( $kg\ kg^{-1}$ )
$q_{ca}$	analyzed cloud water content ( $kg\ kg^{-1}$ )
$q_{cb}$	simulated (background) cloud water content ( $kg\ kg^{-1}$ )
$q_i$	specific cloud ice water content ( $kg\ kg^{-1}$ )
$q_s$	saturated specific humidity ( $kg\ kg^{-1}$ )
$q_{sb}$	simulated (background) saturated specific humidity ( $kg\ kg^{-1}$ )
$q_t$	total water content ( $kg\ kg^{-1}$ )
$q_{tb}$	simulated (background) total water content ( $kg\ kg^{-1}$ )
r	decorrelation distance (m)
$r_e$	effective radius of cloud droplets (m)
<b>R</b>	observation error covariance matrix
$R_s$	incoming shortwave radiation ( $W\ m^{-2}$ )
T	air temperature (K)
z	height (m)
$\delta$	Kronecker delta
$\rho$	air density ( $kg\ m^{-3}$ )
$\rho_w$	density of liquid water ( $kg\ m^{-3}$ )
$\sigma_c$	standard deviation of the background cloud water content
$\sigma_s$	standard deviation of the simulated saturated specific humidity
$\sigma_t$	standard deviation of the simulated total water content
$\sigma_\tau$	standard deviation of the observed cloud optical thickness
$\tau_0$	observed cloud optical thickness (-)
$\tau_b$	simulated (background) cloud optical thickness (-)

2

3

## 1 **Appendix B: Non-diagonal $\mathbf{B}$ matrix**

2 To obtain the formulas in section 3.2, we have assumed that the background error covariance  
3 matrix is diagonal, which ignores the correlation of errors of cloud water content between  
4 different vertical layers. This may have an impact on the resulting cloud water profiles of the  
5 analysis, especially if the layers are close to each other in comparison to the typical thickness  
6 of a cloud layer. In order to have an estimate of the effect of this assumption, a test is  
7 performed with a non-diagonal  $\mathbf{B}$  matrix. In our test, a simple exponential decay of the  
8 correlation of the errors is applied to the off-diagonal elements of  $\mathbf{B}$ , which gives for row  $i$   
9 and column  $j$ :

$$10 \quad \mathbf{B}_{ij} = \sigma_{ci}\sigma_{cj}e^{-\frac{|z_i-z_j|}{r}}$$

11  
12 with  $r$  the vertical decorrelation length.  $r$  is given a value of 2000 m, corresponding to the  
13 value used by Zupanski et al. (2005) for the vertical decorrelation length of total water mixing  
14 ratio in their study on vertical correlations in error covariance modelling.

15  
16 The impact of the non-diagonal  $\mathbf{B}$  matrix on the analyzed cloud water contents for a radio-  
17 sounding profile at Trappes is presented in Figure 9. The non-diagonal matrix has some effect  
18 on the assimilated cloud water profile and mainly spreads out the cloud water peaks.  
19 However, the total amounts and locations of the assimilated cloud water content are  
20 comparable between both experiments. Therefore, we can conclude that the assumption of a  
21 diagonal background error covariance matrix will not have a strong impact on the assimilated  
22 cloud water profiles in this study.

23

## 1 **Appendix C: The uncertainty on the background saturated specific humidity**

2 In the formulation of the error variance of simulated cloud water ( $\sigma_c$ ) in section 3.3, the error  
3 on the background saturated specific humidity (which depends on the error in background  
4 temperature) is assumed to be zero to simplify the assimilation scheme. To assess the  
5 implications of ignoring the error on  $q_s$ , an alternative (and more complex) formulation is  
6 derived here, which takes into account this error. The error variance of simulated cloud water  
7 is now calculated as follows:

8

$$\sigma_c^2 = \langle q_c^2 \rangle - \langle q_c \rangle^2,$$

9

10 with, for  $n = 1, 2$ ,

11

$$\langle q_c^n \rangle = \frac{1}{2\pi\sigma_s\sigma_t} \int_{-\infty}^{+\infty} \int_{q_s}^{+\infty} (q_t - q_s)^n e^{-\left(\frac{q_t - q_{tb}}{\sqrt{2}\sigma_t}\right)^2} e^{-\left(\frac{q_s - q_{sb}}{\sqrt{2}\sigma_s}\right)^2} dq_t dq_s.$$

12

13 In this expression,  $q_{tb}$  and  $q_{sb}$  denote the simulated (background) values of the quantities  $q_t$   
14 (total specific water content) and  $q_s$  (saturated specific humidity content) , which have  
15 assumed known standard deviations  $\sigma_t$  and  $\sigma_s$ , respectively, and which are taken here to be  
16 stochastically independent.

17

18 We first proceed to a transformation of variables by  $x = \frac{(q_t - q_s)}{\sqrt{2}\sigma_t}$ , and also introduce  $x_s =$   
19  $\frac{(q_{tb} - q_s)}{\sqrt{2}\sigma_t}$  and  $x_{sb} = \frac{(q_{tb} - q_{sb})}{\sqrt{2}\sigma_t}$ . Moreover, introducing  $\alpha = \sigma_t/\sigma_s$ , and changing the order of  
20 integration, the integral can be written as:

21

$$\begin{aligned}\langle q_c^n \rangle &= \frac{(\sqrt{2}\sigma_t)^{n+2}}{2\pi\sigma_s\sigma_t} \int_0^{+\infty} x^n \left[ \int_{-\infty}^{+\infty} e^{-(x-x_s)^2} e^{-\alpha^2(x_s+x_{sb})^2} dx_s \right] dx \\ &= \frac{(\sqrt{2}\sigma_t)^{n+2}}{2\sqrt{\pi}\sigma_s\sigma_t} \frac{1}{\sqrt{1+\alpha^2}} \int_0^{+\infty} x^n e^{-\left[\frac{\alpha(x+x_{sb})}{\sqrt{1+\alpha^2}}\right]^2} dx,\end{aligned}$$

1

2 where we made use of one of definite integrals listed in Gradshteyn and Ryzik (2007). After

3 some further algebra, again using integrals listed in Gradshteyn and Ryzik (2007), and

4 introducing  $\sigma_{ts}^2 \equiv \sigma_t^2 + \sigma_s^2$ , it is then fairly straightforward to work out the above integrals,

5 which yields:

6

$$\begin{aligned}\langle q_c \rangle &= \sigma_{ts} \left[ \frac{1}{\sqrt{2\pi}} e^{-x_{sb}^2} - \frac{x_s}{\sqrt{2}} \operatorname{erfc}(x_{sb}) \right] \\ \langle q_c^2 \rangle &= \sigma_{ts}^2 \left[ \frac{1}{\sqrt{\pi}} x_{sb} e^{-x_{sb}^2} - \frac{1}{2} (1 + 2x_{sb}^2) \operatorname{erfc}(x_{sb}) \right],\end{aligned}$$

7

8 The impact of this new formulation, which takes into account the error of  $q_s$ , on the analyzed

9 cloud water contents for a radio-sounding profile at Trappes is presented in Figure 10. For this

10 experiment,  $\sigma_s$  is given a value of 0.2, which corresponds to an uncertainty on the background

11 air temperature of about 3 K. The effect on the assimilated cloud water profile is rather small

12 as only some minor shifts can be noticed. The total amounts and locations of the assimilated

13 cloud water content are very similar between both experiments. Therefore, we can conclude

14 that the assumptions that are made in section 3.3 are not likely to have a significant impact on

15 the results of this study.

16

1   **REFERENCES**

2   Albers, S.C., McGinley, J.A., Birkenheuer, D.A. and Smart, J.R. 1996. The Local Analysis  
3   and Prediction System (LAPS): Analysis of clouds, precipitation and temperature. *Weather*  
4   *Forecasting*, 11, 273-287.

5

6   Benedetti, A., Stephens, G.L., and Vukićević, T., 2003. Variational assimilation of radar  
7   reflectivities in a cirrus model. I: Model description and adjoint sensitivity studies. *Quart. J.*  
8   *Roy. Meteor. Soc.*, 129, 277–300.

9

10   Benedetti, A. and Janisková, M. 2008. Assimilation of MODIS Cloud Optical Depths in the  
11   ECMWF Model. *Atmospheric Review*, 136, 1727-1747.

12

13   Brewster, K. 1996. Application of a Bratseth analysis scheme including Doppler radar data.  
14   Preprints, 15th Conf. Wea. Anal. Forecast. Amer. Meteor. Soc., Norfolk, VA, pp 92–95.

15

16   DeRidder, K. and Schayes, G. 1997. The IAGL land surface model. *Journal of Applied*  
17   *Meteorology*, 36, 167-182.

18

19   Gradshteyn, I. S. and Ryzhik, I. M. 2007. *Table of Integrals, Series and Products*, Seventh  
20   Edition. Academic Press, 1161 pp.

21

22   Hu, M., Xue, M. and Brewster, K. 2006a. 3D-VAR and cloud analysis with WSR-88D level-  
23   II data for the prediction of the Fort Worth, Texas, tornadic thunderstorms. Part I: Cloud  
24   analysis and its impact. *Mon. Wea. Rev.*, 134, 675–698.

25

1 Hu, M., Xue, M. and Brewster, K. 2006b. 3D-VAR and cloud analysis with WSR-88D level-  
2 II data for the prediction of the, Fort Worth, Texas, tornadic thunderstorms. Part II: Impact of  
3 radial velocity analysis via 3D-VAR. *Mon. Wea. Rev.*, 134, 699–721.  
4

5 Kain, J. S. and Fritsch, J.M. 1990. A One-Dimensional Entraining Detraining Plume Model  
6 and Its Application in Convective Parameterization. *Journal of the Atmospheric Sciences*, 47,  
7 2784-2802.  
8

9 Kalnay, E. 2003. *Atmospheric modeling, data assimilation and predictability*. Cambridge  
10 Univ. Press, 341 pp.  
11

12 Kokhanovsky, A. A., Rozanov, V.V., Zege, E.P., Bovensmann, H. and Burrows, J.P. 2003. A  
13 semi-analytical cloud retrieval algorithm using backscattered radiation in 0.4- 2.4 $\mu$ m spectral  
14 region, *J. Geophys. Res.*, 108, 10.1029/2001JD001543.  
15

16 Kokhanovsky, A. A. 2006. *Cloud Optics*, Berlin: Springer-Verlag.  
17

18 Lin, Y.-L., Farley, R.D. and Orville, H.D. 1983. Bulk parameterization of the snow field in a  
19 cloud model. *J Climate Appl Meteor*, 22, 1065-1092.  
20

21 Pandey, P., De Ridder, K. and van Lipzig, N.P.M. 2011. Estimating scaled cloud optical  
22 thickness from SEVIRI by implementing a semi-analytical cloud retrieval algorithm.  
23 *Atmospheric Research*, in review.  
24

1 Soutu, M.J., Balseiro, C.F., Pérez-Munuzuri, V., Xue, M. and Brewster, K. 2003. Impact of  
2 Cloud Analysis on Numerical Weather Prediction in the Galician Region of Spain. *Journal of*  
3 *Applied Meteorology*, 42, 129-140.  
4  
5 Sun, W. Y. and Chang, C.Z. 1986. Diffusion-Model for a Convective Layer .1. Numerical-  
6 Simulation of Convective Boundary-Layer. *Journal of Climate and Applied Meteorology*, 25:  
7 1445-1453.  
8  
9 Sun, J. and Crook, N.J. 1998. Dynamical and microphysical retrieval from Doppler radar  
10 observations using a cloud model and its adjoint. Part II: Retrieval experiments of an observed  
11 Florida convective storm. *J. Atmos. Sci.*, 55, 835–852.  
12  
13 Vukićević, T., Greenwald, T., Županski, M., Županski, D., Vonder Haar, T. and Jones, A.S.  
14 2004. Mesoscale cloud state estimation from visible and infrared satellite radiances. *Mon.*  
15 *Wea. Rev.*, 132, 3066–3077.  
16  
17 Xue, M. 2000. High-order monotonic numerical diffusion and smoothing. *Monthly Weather*  
18 *Review*, 128, 2853-2864.  
19  
20 Xue, M., Droegemeier, K.K. and Wong, V. 2000. The Advanced Regional Prediction System  
21 (ARPS) - A multi-scale nonhydrostatic atmospheric simulation and prediction model. Part I:  
22 Model dynamics and verification. *Meteorology and Atmospheric Physics*, 75, 161-193.  
23  
24 Xue, M., Droegemeier, K.K., Wong, V., Shapiro, A., Brewster, K., Carr, F., Weber, D., Liu,  
25 Y. and Wang, D. 2001. The Advanced Regional Prediction System (ARPS) - A multi-scale

1 nonhydrostatic atmospheric simulation and prediction tool. part II: Model physics and  
2 applications. *Meteorology and Atmospheric Physics*, 76, 143-165.

3

4 Yucel, I., Shuttleworth, W.J., Gao, X. and Sorooshian, S. 2003. Short-term Performance of  
5 MM5 with Cloud-Cover Assimilation from Satellite Observations. *Monthly Weather Review*  
6 131, 1797-1810.

7

8 Zupanski, M., Zupanski, D., Vukicevic, T., Eis, K. and Vonder Haar, T. 2005. CIRA/CSU  
9 Four-Dimensional Variational Data Assimilation System. *Monthly Weather Review* 133, 829-  
10 843.

11

1 **TABLES**

2 Table 1: Statistics of the 2 m air temperature for the entire month of June 2006.

<b>T (°C)</b>	<b>Mean</b>	<b>Bias</b>	<b>RMSE</b>	<b>R<sup>2</sup></b>
<b>Melun</b>				
Obs	18.06	/	/	/
REF	18.59	0.53	2.64	0.85
EXP	18.01	-0.05	1.94	0.89
<b>Grignon</b>				
Obs	17.18	/	/	/
REF	18.52	1.34	2.95	0.84
EXP	17.84	0.66	2.14	0.87
<b>Oensingen</b>				
Obs	15.83	/	/	/
REF	16.13	0.30	3.42	0.79
EXP	15.28	-0.55	2.84	0.80
<b>Bordeaux</b>				
Obs	21.27	/	/	/
REF	21.11	-0.16	3.09	0.84
EXP	20.53	-0.74	2.52	0.88

3

4

5

1 Table 2: Statistics of the incoming shortwave radiation for the entire month of June 2006.

<b>Rs (W m<sup>-2</sup>)</b>	<b>Mean</b>	<b>Bias</b>	<b>RMSE</b>	<b>R<sup>2</sup></b>
<b>Grignon</b>				
Obs	360.30	/	/	/
REF	416.12	55.82	156.35	0.77
EXP	400.72	40.42	124.02	0.84
<b>Fontainbleau</b>				
Obs	381.90	/	/	/
REF	430.69	48.79	157.24	0.77
EXP	410.46	28.56	119.35	0.85
<b>Oensingen</b>				
Obs	311.84	/	/	/
REF	360.75	48.91	168.43	0.77
EXP	344.00	22.16	140.24	0.83

2

3

1 Table 3: Statistics of the 2 m specific humidity for the entire month of June 2006.

<b>q (g kg<sup>-1</sup>)</b>	<b>Mean</b>	<b>Bias</b>	<b>RMSE</b>	<b>R<sup>2</sup></b>
<b>Melun</b>				
Obs	8.67	/	/	/
REF	8.70	0.03	1.35	0.56
EXP	9.62	0.95	1.89	0.50
<b>Grignon</b>				
Obs	8.67	/	/	/
REF	8.64	-0.03	1.26	0.58
EXP	9.44	0.77	1.66	0.54
<b>Oensingen</b>				
Obs	9.68	/	/	/
REF	8.67	-1.01	2.13	0.67
EXP	9.41	-0.27	1.76	0.71
<b>Bordeaux</b>				
Obs	8.96	/	/	/
REF	8.82	-0.14	1.26	0.69
EXP	9.85	0.89	1.62	0.66

2

3

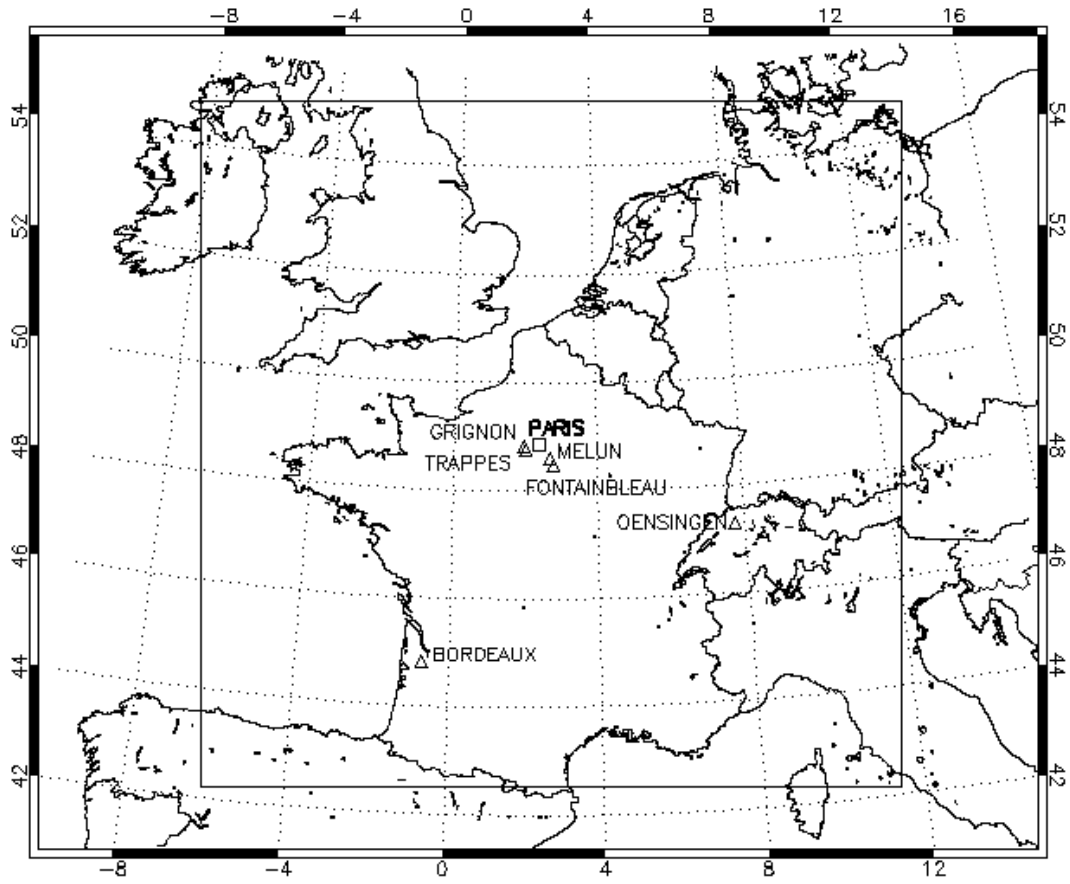
1 Table 4: Statistics for Melun for all the sensitivity experiments.

	<b>Obs</b>	<b>REF</b>	<b>EXP</b>	<b>a=0.1</b>	<b>a=0.5</b>	<b>b=0.1</b>	<b>b=0.5</b>
T (°C)	18.06	18.59	18.01	18.10	16.19	16.57	18.03
RMSE	/	2.64	1.94	2.44	3.04	2.51	1.97
R <sup>2</sup>	/	0.85	0.89	0.86	0.82	0.86	0.88
q (g kg <sup>-1</sup> )	8.67	8.70	9.62	9.18	10.30	10.13	9.61
RMSE	/	1.35	1.89	1.60	2.78	2.65	1.88
R <sup>2</sup>	/	0.56	0.50	0.51	0.41	0.44	0.50

2

3

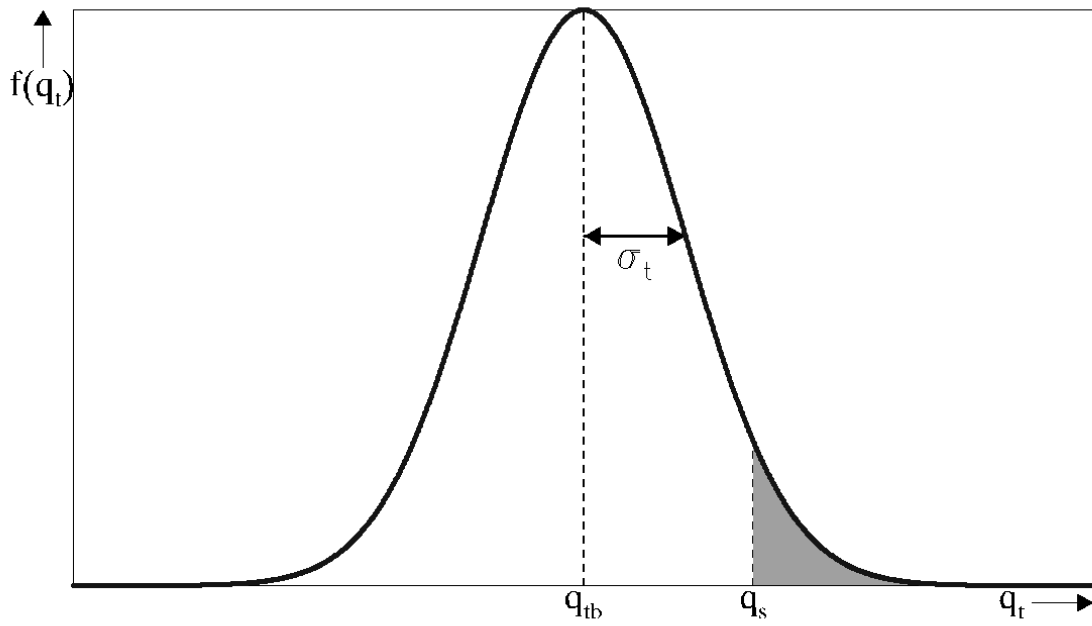
1 FIGURES



2

3 Figure 1: Location of the model domain and the observational stations.

4



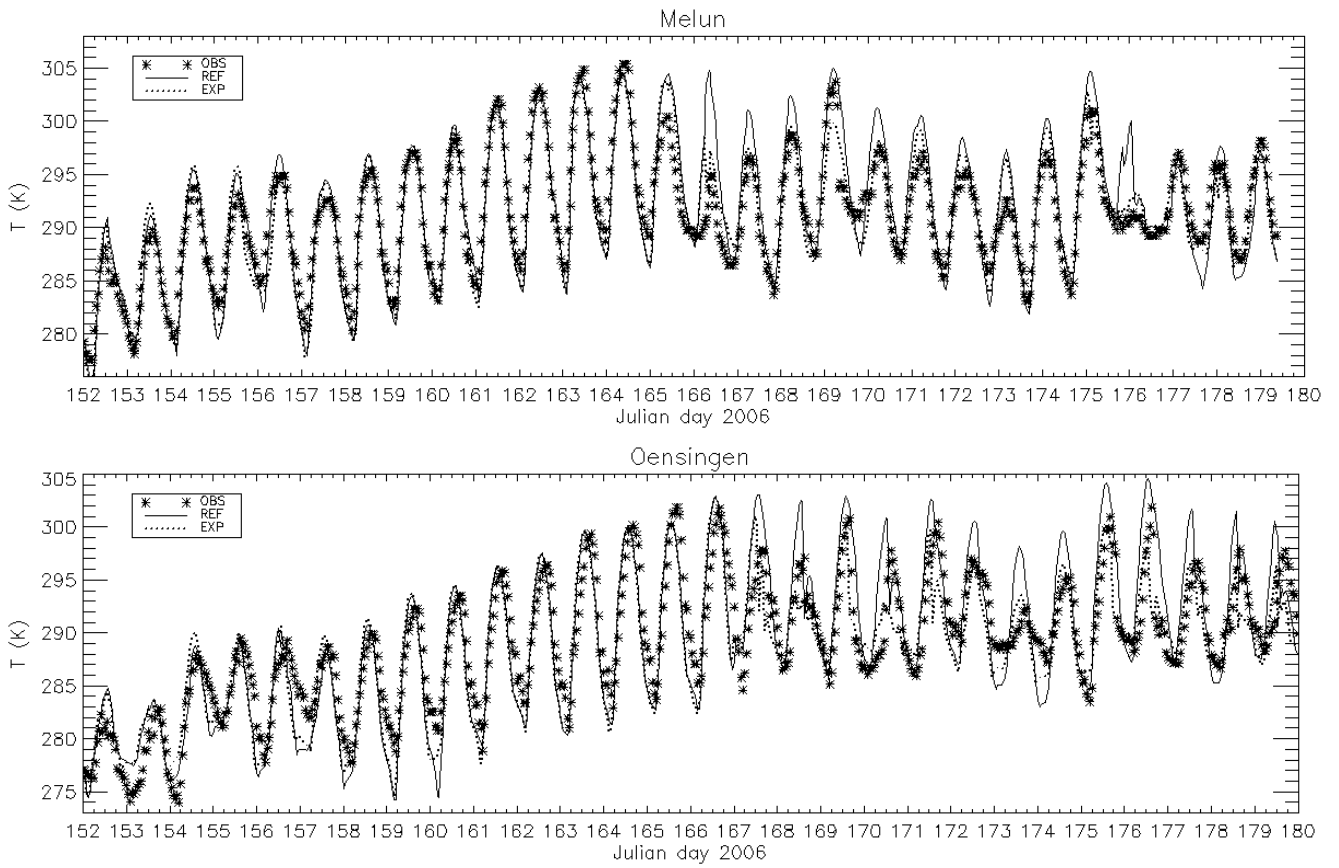
1

2 Figure 2. Probability distribution function for total water content (blue line), with expectation  
 3 value  $q_{tb}$ , and standard deviation  $\sigma_t$ . The light shading corresponds to the area above the  
 4 saturated specific humidity (denoted  $q_s$ ), which contains cloud water.

5

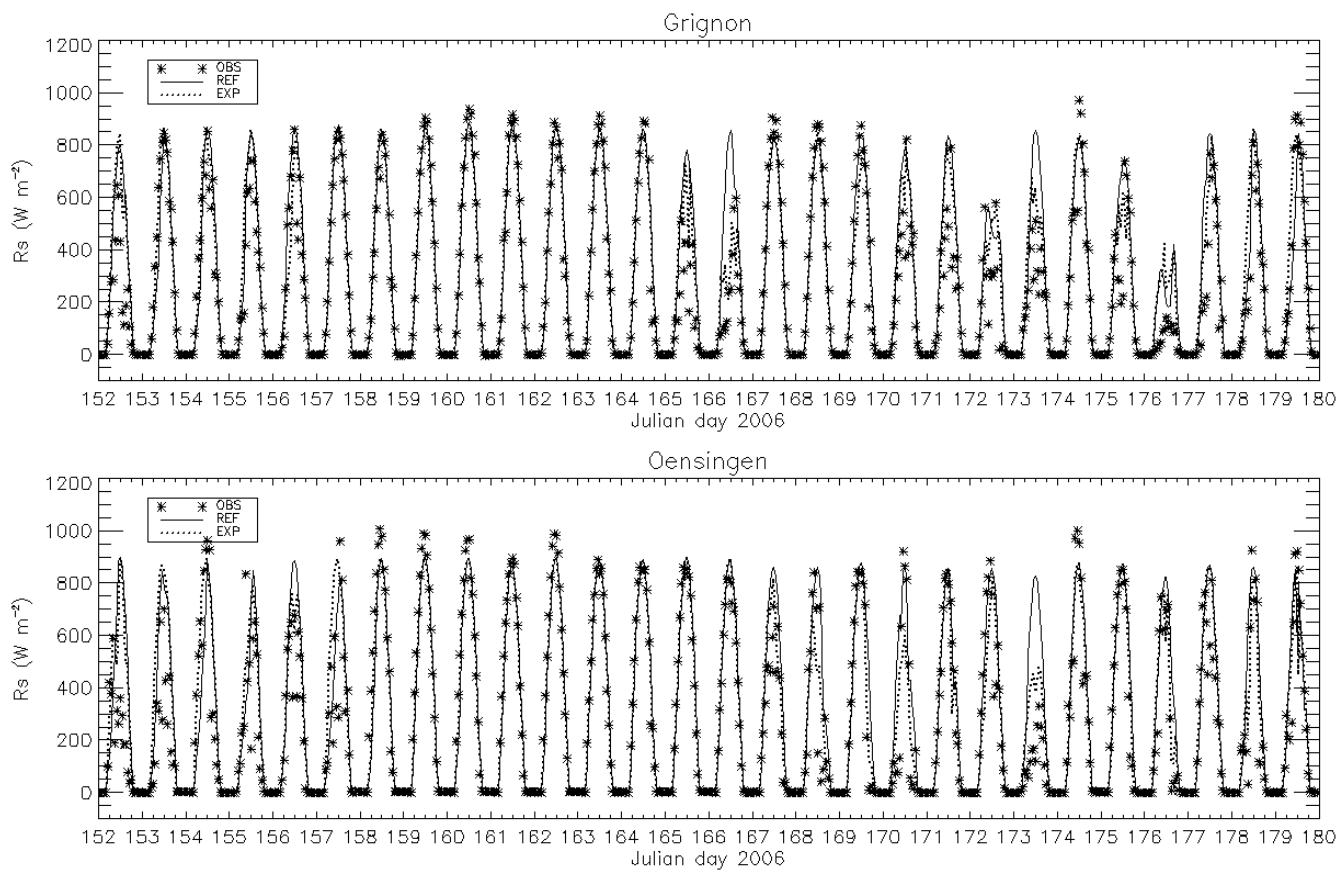
6

7



3  
 4 Figure 3: 2 m air temperature at Melun (upper panel) and Oensingen (lower panel) for June  
 5 2006.

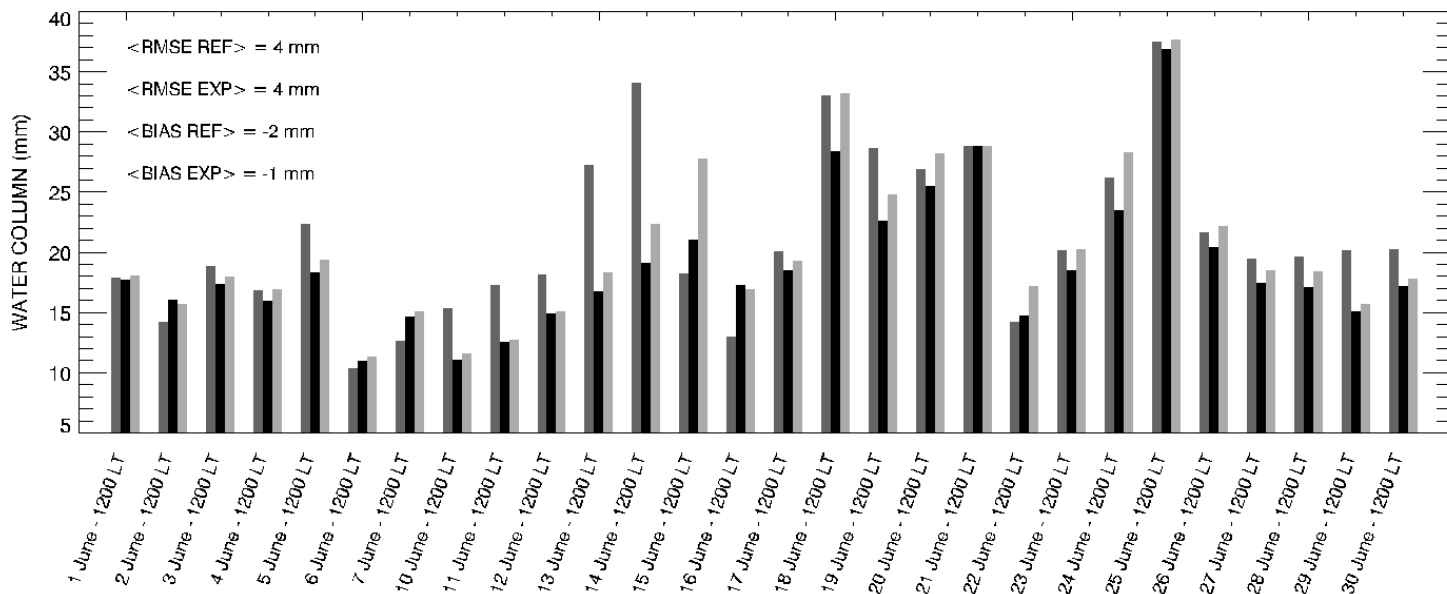
6  
 7  
 8



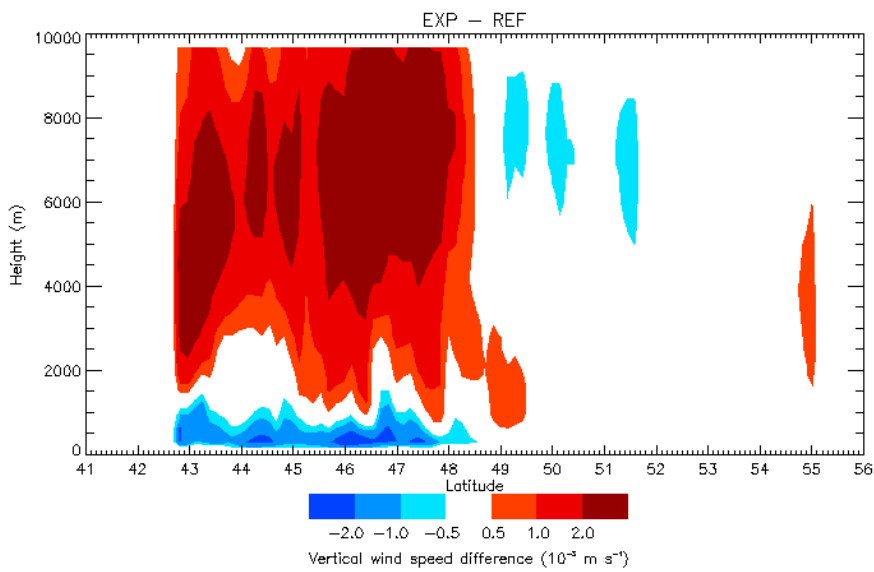
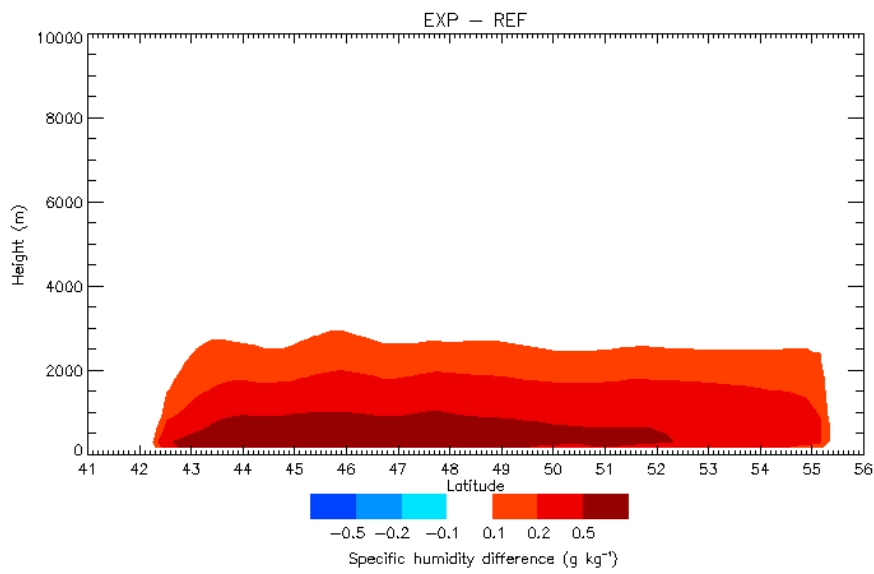
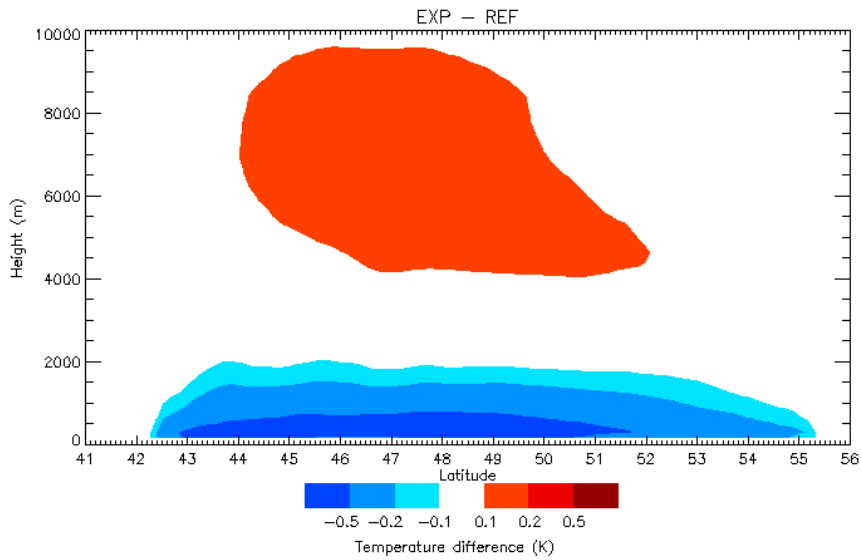
3  
 4 Figure 4: Incoming shortwave radiation at Grignon (upper panel) and Oensingen (lower  
 5 panel) for June 2006.

6  
 7

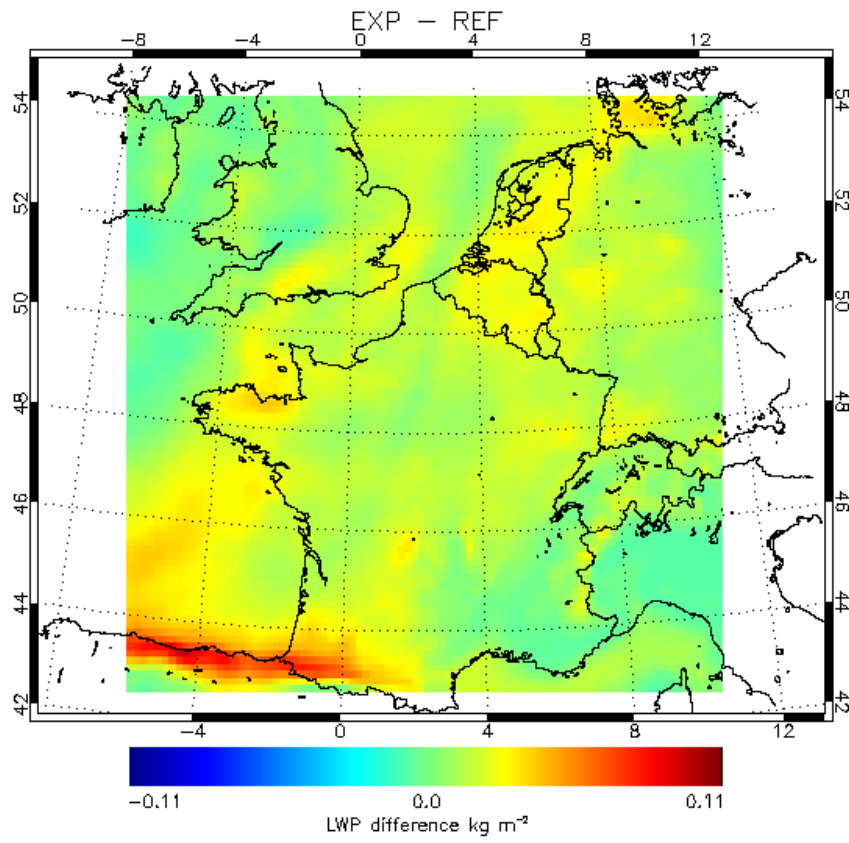
### WATER COLUMN AT TRAPPES



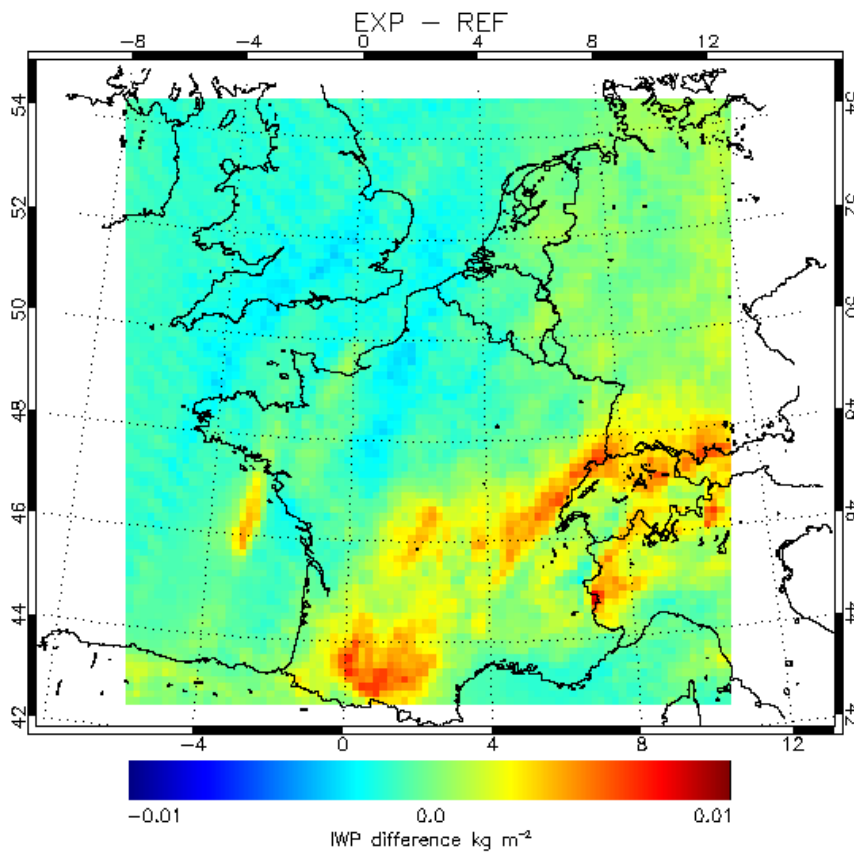
2  
3 Figure 5: The water column at Trappes from radio-sounding measurements (dark grey bars),  
4 the Reference simulation (black bars) and the COT assimilation experiment (light grey bars).  
5  
6  
7



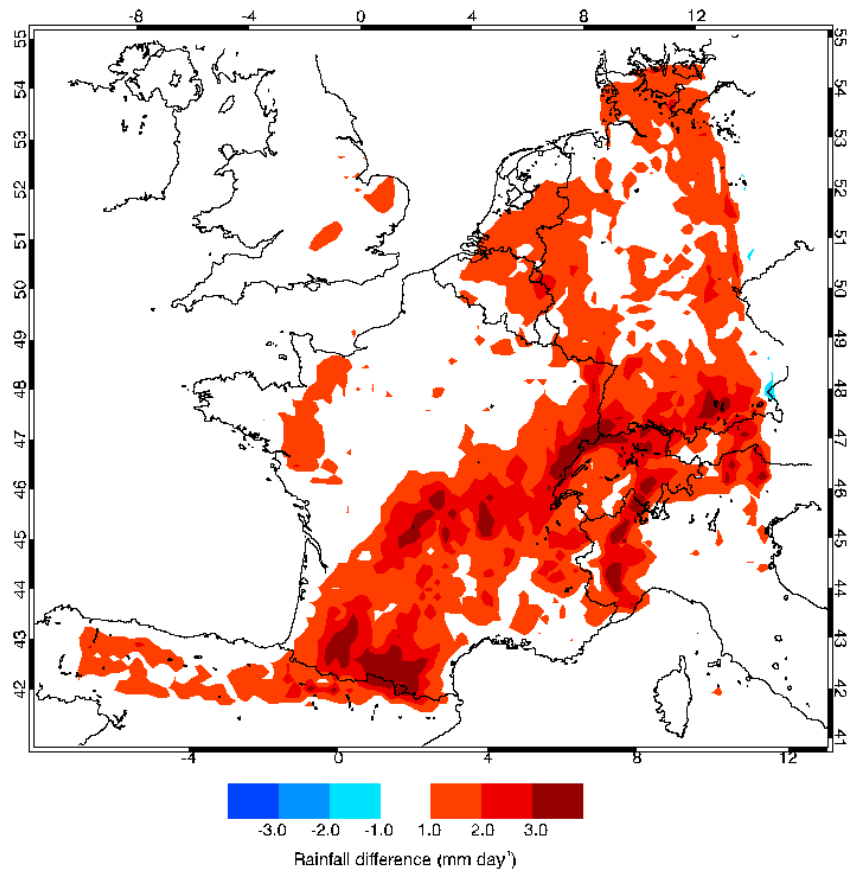
5 Figure 6: Monthly mean differences between the COT assimilation experiment and the  
6 Reference simulation, averaged per latitude band.



1

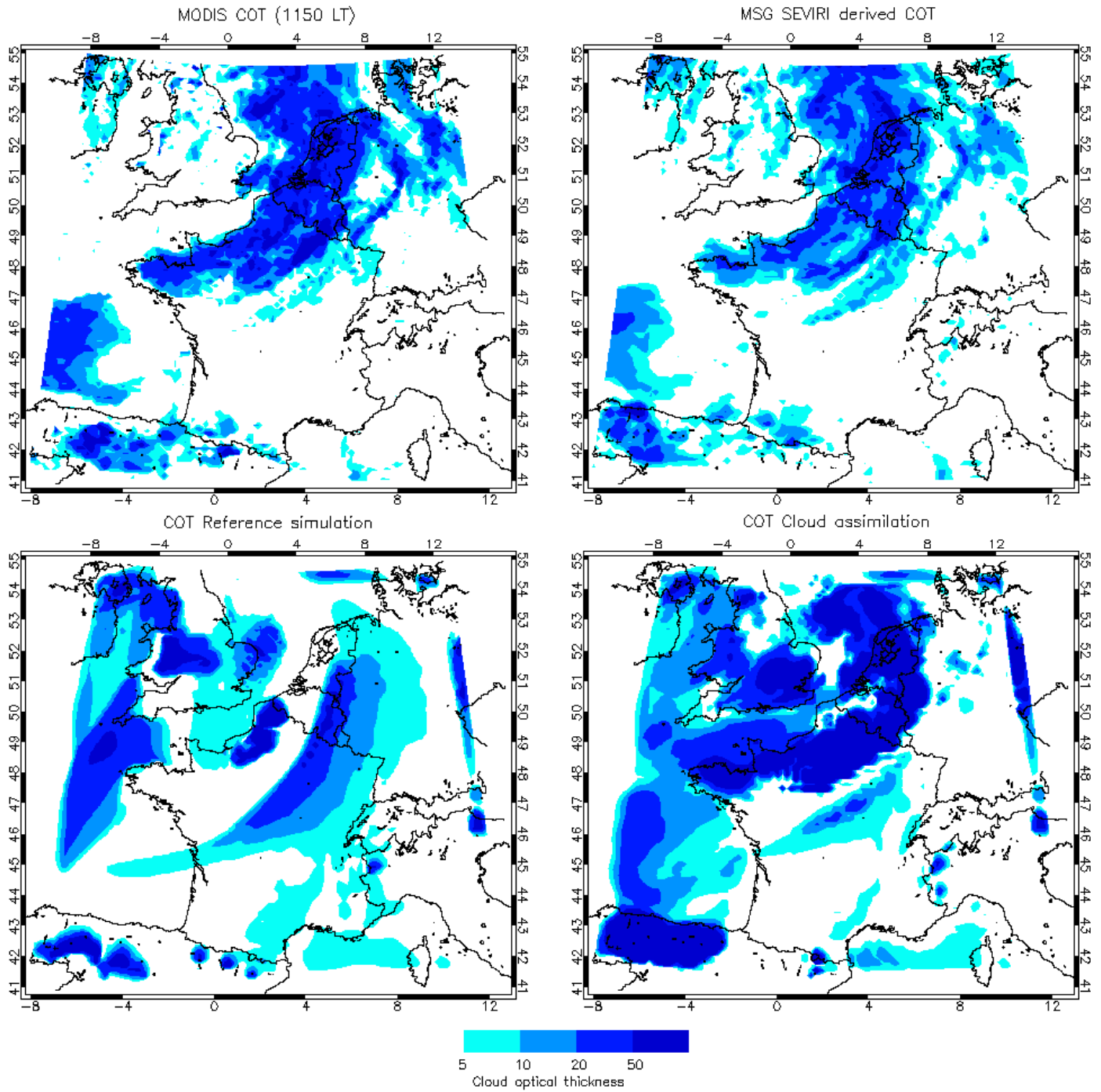


2



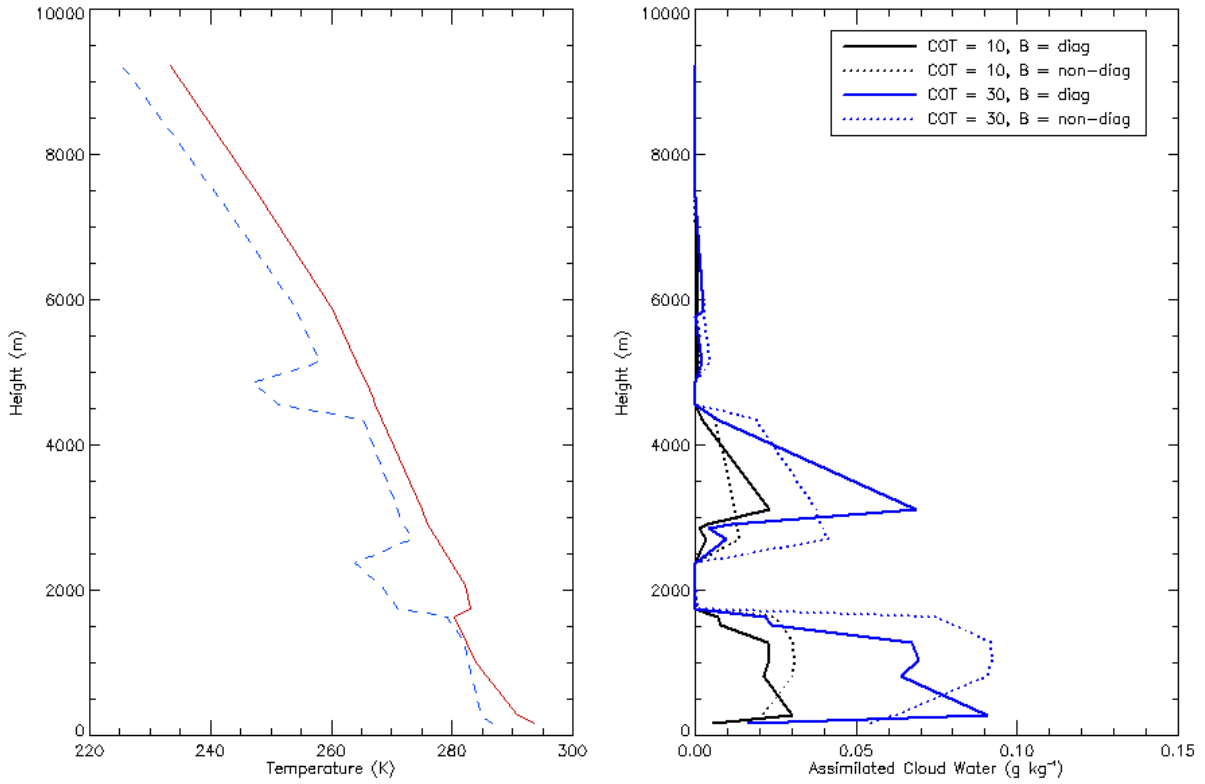
1  
2  
3  
4  
5

Figure 7: Monthly mean differences in liquid water path (upper panel), ice water path (middle panel) and rainfall amounts (lower panel) between the COT assimilation experiment and the Reference simulation.



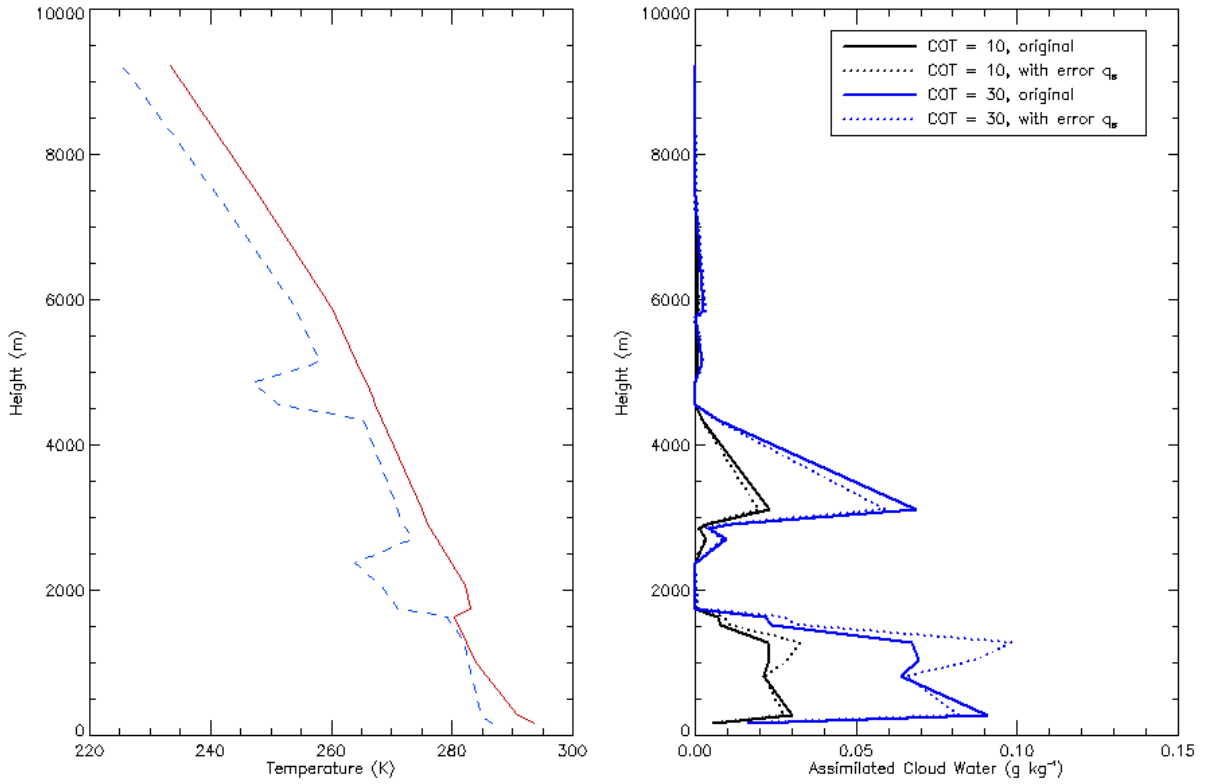
2  
3  
4

Figure 8: Cloud optical thickness maps on 15 June 2006 at 1200 LT.



1  
2  
3  
4  
5  
6  
7

Figure 9: Left: Radio-sounding profile of temperature (red) and dew point temperature (blue) at Trappes on 20 June at 1200 LT. Right: Resulting cloud water profiles from experiments with a non-diagonal B matrix.



1  
2  
3  
4  
5  
6

Figure 10: Left: Radio-sounding profile of temperature (red) and dew point temperature (blue) at Trappes on 20 June at 1200 LT. Right: Resulting cloud water profiles from experiments including the uncertainty in the background saturated specific humidity.